RSC Advances

PAPER

View Article Online
View Journal | View Issue

Cite this: *RSC Adv.*, 2022, **12**, 25081

A controllable one-pot hydrothermal synthesis of spherical cobalt ferrite nanoparticles: synthesis, characterization, and optical properties

Nedaa M. Refat,[a] Mostafa Y. Nassar *[b] and Sadeek A. Sadeek*[a]

We herein report the controllable synthesis of spherical cobalt ferrite nanoparticles with average crystallite size in the range of 3.6–12.9 nm using a facile, eco-friendly, hydrothermal method. The hydrothermal treatment was carried out by utilizing cobalt nitrate, ferric nitrate, and ammonium hydroxide in the presence and absence of Arabic gum as a surfactant agent. The purity and crystallinity of the products were tuned by varying reaction conditions such as reaction time (0.5–8 h), reaction temperature (120–180 °C), percentage of ethylene glycol (0–100% (v/v)), pH (8–9.6), and amount of Arabic gum (0–2 g). We characterized the prepared products using X-ray diffraction (XRD), field-emission scanning electron microscopy (FE-SEM), Fourier transform infrared spectroscopy (FT-IR), high-resolution transmission electron microscopy (HR-TEM), energy-dispersive X-ray spectroscopy analysis (EDS), selected area electron diffraction (SAED) patterns, and UV-visible diffuse reflectance spectra (DRS). The optimal hydrothermal treatment was performed at 180 °C and pH 9.6 for 4 h in aqueous media. The results also revealed that the as-prepared spinel cobalt ferrite nanoparticles have an estimated optical band gap energy in the range of *ca.* 1.6–1.9 eV, indicating the semiconducting characteristics of the products.

Received 28th May 2022
Accepted 25th August 2022

DOI: 10.1039/d2ra03345c

rsc.li/rsc-advances

1. Introduction

Spinel ferrite nanoparticles have recently attracted significant attention from researchers owing to their wide range of applications in different fields like catalysts, refractory materials, microwave absorbing materials, biomedical materials, high-frequency magnetic materials, electrical devices, antibacterial materials, gas sensors, water decontaminants, and energy materials.[1–8] Spinel ferrites have the general formula of $(M)^{A}(Fe_2)^{B}O_4$, where M stands for divalent metal cations such as Co, Ni, Mg, Mn, Cu, Zn, Cd, *etc.* Their properties are attributed to the cation distribution because of the existence of altered distribution of cations in A (tetrahedral site (T_d)) and B (octahedral site (O_h)) sites.[5] The spinel ferrite structures depend mainly on the cation distribution, so they are categorized into three types: normal, inverse, and mixed spinels.[9–11] Because of its excellent mechanical hardness, high chemical stability, and distinctive electrical, magnetic, and optical properties, $CoFe_2O_4$ has received a lot of attention among ferrites. Cobalt ferrite has thus been applied for various applications including catalysis, microwave devices, data storage, drug delivery, magnetic resonance imaging, ferrofluid recording media, gas sensors, water treatment, and lithium-ion rechargeable batteries.[2,12–16]

Cobalt ferrite nanoparticles have been synthesized using various synthesis methods such as mechanical milling, laser ablation, co-precipitation, plasma synthesis, hydrothermal, auto-combustion, microwave, sol–gel, and microemulsion.[14,17,18] Choice of the synthetic route and the applied reaction conditions have a great impact on the characteristics of the produced $CoFe_2O_4$ nanoparticles such as morphology, crystallinity, surface area, as well as chemical and physical properties.[17,18] Among the synthesis routes, hydrothermal synthesis is a controllable, facile, eco-friendly, and energy-efficient route for the synthesis of pure $CoFe_2O_4$ nanoparticles with tunable particle size.[14,19–21] However, a significant number of the published reports claimed that $CoFe_2O_4$ NPs were prepared in a two-step process; where the hydrothermally prepared precursors were subsequently thermally treated to produce $CoFe_2O_4$ NPs. In this light, Bastianello and his colleagues prepared $CoFe_2O_4$ NPs *via* a hydrothermal method at 135 °C for 72 h and investigated the effect of the calcination at different temperatures on the electronic conduction properties.[22] Anila *et al.* prepared cobalt ferrite nanoparticles using a hydrothermal technique at 180 °C for 12 h, and then the final products were obtained by annealing at 550 °C. Nassar *et al.* synthesized cobalt ferrite nanoparticles *via* a hydrothermal technique by hydrothermal preparation of nanocomposites of cobalt and iron carbonates followed by their thermal decomposition.[14] On the other hand, Zhijun *et al.* prepared cobalt ferrite nanoparticles by rapid mixing metal cations with sodium borohydride as a reducing agent and simultaneous reduction in a colloid mill at

[a]*Chemistry Department, Faculty of Science, Zagazig University, Zagazig, Egypt. E-mail: s_sadeek@zu.edu.eg; Tel: +20 1220057510*

[b]*Chemistry Department, Faculty of Science, Benha University, Benha 13518, Egypt. E-mail: m_y_nassar@yahoo.com; m_y_nassar@fsc.bu.edu.eg; Tel: +20 1068727555*

6000 rpm for 2 min, then the produced slurry was transferred to an autoclave at 120 °C for 12 h.[23] Besides, Guangbin and coworkers hydrothermally synthesized $CoFe_2O_4$ NPs at 130 °C for 15 h in the presence of cetyltrimethylammonium bromide (CTAB) as a surfactant.[24] Varma *et al.* have studied the preparation of $CoFe_2O_4$ NPs by solid state, citrate precursor, and polymerized complex methods.[25] However, to the best of our knowledge, we have not noticed a detailed investigation about tuning the morphology, phase purity, and particle size of cobalt ferrite nanoparticles *via* a one-pot hydrothermal method without subsequent heat treatment. This prompted us to explore extensively the preparation of $CoFe_2O_4$ NPs by developing a one-pot, time-saving hydrothermal route without further annealing or using complex equipment. Moreover, exploring the growth mechanism of the prepared cobalt ferrite particles is crucial for practical use.

Herein, in the present work, we have developed a one-pot, facile, and eco-friendly method for the synthesis of cobalt ferrite nanoparticles by hydrothermal treatment of ammonical solutions of cobalt and iron nitrates in 4 h without subsequent heat treatment or complex equipment. Various factors influencing the hydrothermal process such as reaction temperature, reaction time, ethylene glycol : water ratio, pH, and the amount of Arabic gum have been investigated. Additionally, we have explored the growth mechanism of the prepared cobalt ferrite particles. We have characterized the morphology, composition, crystallite size, and band gap of the products by using XRD, FE-SEM, HR-TEM, SAED, EDS, FT-IR spectra, and UV-visible diffuse reflectance (DRS).

2. Experimental

2.1 Materials and reagents

Ferric nitrate ($Fe(NO_3)_3 \cdot 9H_2O$) and ethylene glycol (EG) were purchased from Sd Fine-Chem. Limited (SDFCL), India. Cobalt nitrate ($Co(NO_3)_2 \cdot 6H_2O$) was bought from Alpha Chemika, India. El-Nasr Pharmaceutical Chemicals company (ADWIC), Egypt supplied us with an ammonia solution (25%), ethanol (70%), and sodium hydroxide pellets. Arabic gum (AG) was obtained from LOBA Chemie, India. All of the materials and reagents were utilized as received with no further purification.

2.2 Preparation of cobalt ferrite nanoparticles

Cobalt ferrite nanoparticles were synthesized by a hydrothermal method. This was performed by dissolving ferric nitrate (6.4 g, 15.84 mmol, 2 eq.) and cobalt nitrate (2.305 g, 7.92 mmol, 1 eq.), separately, in 40 mL EG, then both solutions were mixed with stirring. The produced solution was heated at 70 °C. To the heated and stirring solution, an aqueous ammonia solution (3 M, 50 mL) was added dropwise. Afterward, the brown reaction blend was allowed to stir for 30 min at 70 °C then transferred to a Teflon-lined autoclave. The autoclave was then sealed and placed in an oven set up at 180 °C for 4 h. After the autoclave was allowed to get the ambient temperature naturally, the black precipitate was separated and washed with bi-distilled water and ethanol (70%) until the pH value of the washing became neutral. The separated precipitate was dried at 100 °C for *ca.* 5 h in an electric oven. For comparison, a sample was prepared using similar conditions except for the hydrothermal treatment step. The produced sample was denoted as CF. On the other hand, we studied the effects of several parameters on the hydrothermal experiment such as (a) reaction time (0.5, 4, and 8 h); (b) temperature (180, 150, and 120 °C); (c) the amount of EG (100%, 75%, 50%, 25%, 0% (v/v)); (d) the pH value by using ammonia solution (9.6, 9, and 8); and (e) the amount of AG (0.5, 1, and 2 g). The hydrothermally prepared samples were referred to as listed in Table 1. The preparation method is outlined in Scheme 1. The proposed reaction mechanism for the formation of cobalt ferrite nanoparticles is presented in Scheme 2.

2.3 Characterization of cobalt ferrite nanoparticles

The crystallographic studies of $CoFe_2O_4$ NPs were obtained using an X-ray powder diffractometer (Bruker Co. D8 Advanced) with Cu Kα radiation source ($\lambda = 1.5406$ Å), a generator voltage of 40 kV and 40 mA generator current (Central Metallurgical R&D Institute Cairo, Egypt). The powder sample was scanned over a 2θ range of 10–80° at a scanning rate of 0.02°/0.4 s. Fourier transform infrared (FT-IR) spectra were obtained using (Thermo Fisher, Nicolet IS10) spectrometer (Mansoura University, Faculty of Science, Mansoura, Egypt). The FT-IR spectra of the prepared samples were recorded at room temperature in the range from 4000 to 400 cm^{-1} to characterize the bond formation and functional groups of the samples under investigation. The morphology characteristics of cobalt ferrite nanoparticles and their texture were examined by HR-TEM analysis and SAED patterns. The high-resolution transmission electron microscopy (HR-TEM) as well as the corresponding selected area electron diffraction (SAED) were performed by a (JEOL, JEM-2100) electron microscope equipped with a high-resolution gun, operated at an acceleration voltage of 200 kV (Nanotech Center, Dreamland, Cairo, Egypt). For the HR-TEM images, aqueous suspensions of the samples were ultrasonicated for 15 min then the samples were deposited on a carbon film supported on a copper grid. The morphology and the energy-dispersive X-ray spectroscopy (EDS) analysis for prepared samples were also investigated using field Emission Scanning Electron Microscope (FE-SEM) (Thermo Scientific, Quattro S, Field Emission Gun (FEG)) (Nanotechnology Research Center, British University, Cairo, Egypt). The UV-vis diffuse reflectance spectra of prepared products were performed in the range of 200–1200 nm by using a UV-vis spectrophotometer (Jasco, Model v670) connected to an integral sphere (Jasco, Model ISN-723; Benha University, Egypt).

3. Results and discussion

3.1 Synthesis and characterization of $CoFe_2O_4$ nanostructures

3.1.1. Synthesis of $CoFe_2O_4$ nanostructures. $CoFe_2O_4$ nanoparticles were synthesized using a facile, one-pot, hydrothermal method. This was performed by hydrothermal treatment of inexpensive materials such as iron nitrate, cobalt

Table 1 Symbols and D_{XRD} values of the hydrothermally prepared samples

Sample	Factor under study	D_{XRD} (nm)	Sample	Factor under study	D_{XRD} (nm)
CF-0.5	0.5 h	3.6	CF-EG25	25% EG	8.5
CF-4	4 h	7.8	CF-W	Water	12.9
CF-8	8 h	8.5	CF-W-9.6	3 M, 50 mL	12.9
CF-180	180 °C	7.8	CF-W-9	3 M, 36 mL	12.7
CF-150	150 °C	6.1	CF-W-8	3 M, 30 mL	12.3
CF-120	120 °C	4.5	CF-AG-0	Without AG	12.9
CF-EG100	100% EG	7.8	CF-AG-0.5	0.5 g AG	12.4
CF-EG75	75% EG	8.1	CF-AG-1	1 g AG	12.1
CF-EG50	50% EG	8.4	CF-AG-2	2 g AG	11.1

nitrate, and ammonia solution for a relatively short time without subsequent thermal treatment. The products of the hydrothermal treatment were tuned by studying various experimental conditions affecting the hydrothermal reactions like the reaction time, temperature, amount of EG, pH value, and amount of AG. The optimization process of the hydrothermal treatment was mainly studied using the XRD technique, as will be discussed shortly. The crystallite sizes (D_{XRD}) of the produced $CoFe_2O_4$ products of the optimization process are tabulated in Table 1. Several other techniques such as FE-SEM, TEM, FT-IR, UV-vis, and DRS were used to characterize the products.

3.1.2. Effect of reaction time. We have investigated the influence of the reaction time of the hydrothermal treatment on the preparation process of cobalt ferrite nanoparticles. The XRD patterns of the products generated at various hydrothermal treatment periods are shown in Fig. 1. The distinctive Bragg diffraction peaks of all the hydrothermal treatment samples are well indexed at 2θ values of 18.2° (111), 30.08° (220), 35.4° (311), 43.05° (400), 53.4° (422), 56.9° (511), 62.5° (440), and 74.01° (533). These peaks correspond to database reference pattern JCPDS card no. 022-1086 (ref. 26) with a cubic spinel structure of cobalt ferrite, space group of *Fd3m* (227), and lattice parameters of $a = b = c = 8.39$ Å, $a = \beta = \gamma = 90$. We have not detected peaks from other crystalline impurities. As depicted in Fig. 1, increasing the hydrothermal reaction time from 0.5 to 8 h brought about enhancing the sharpness and narrowness of the XRD reflection peaks of the products. It can be concluded that the longer the hydrothermal period of the reactions, the more the crystallinity of the products. The average crystallite sizes

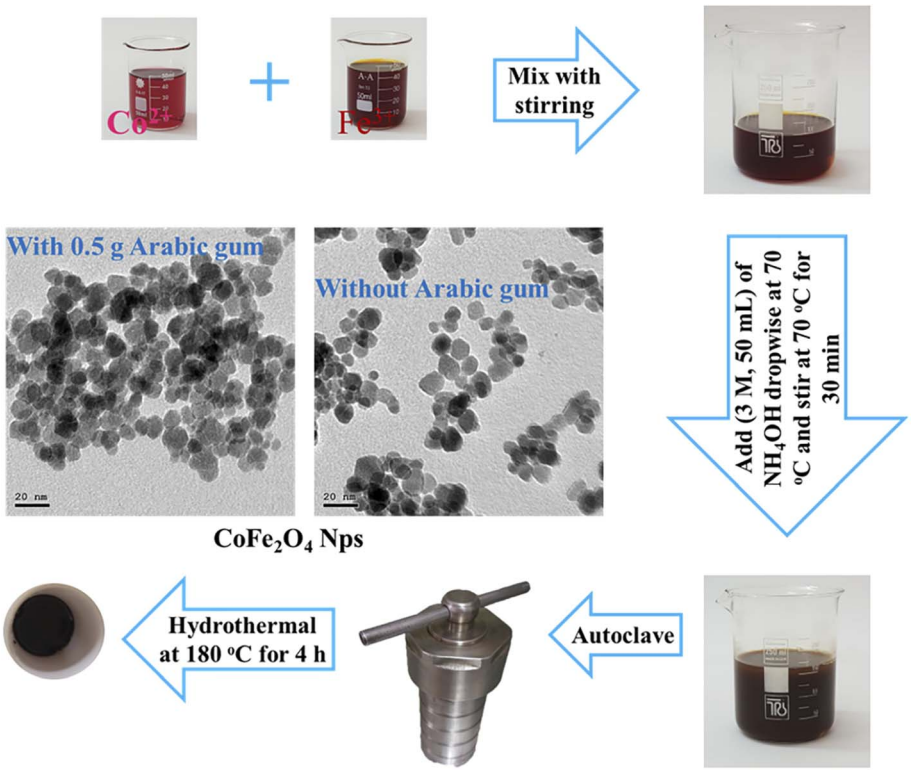

Scheme 1 Preparation of cobalt ferrite nanoparticles by hydrothermal method.

$$Co(NO_3)_2.6H_2O_{(s)} \xrightarrow{H_2O} [Co(H_2O)_6]^{2+}_{(aq)} + 2NO_3^-{}_{(aq)} \quad (1)$$

$$Fe(NO_3)_3.9H_2O_{(s)} \xrightarrow{H_2O} [Fe(H_2O)_6]^{3+}_{(aq)} + 3NO_3^-{}_{(aq)} + 3H_2O \quad (2)$$

$$[Co(H_2O)_6]^{2+}_{(aq)} \xrightarrow{NH_4OH} [Co(OH)_x]^{2-x}_{(aq)} \xrightarrow{NH_4OH} Co(OH)_{2\,(s)} \xrightarrow{NH_4OH} [Co(OH)_3]^-_{(aq)} \quad (3)$$

$$[Fe(H_2O)_6]^{3+}_{(aq)} \xrightarrow{NH_4OH} [Fe(OH)_y]^{3-y}_{(aq)} \xrightarrow{NH_4OH} Fe(OH)_{3\,(s)} \xrightarrow{NH_4OH} [Fe(OH)_4]^-_{(aq)} \quad (4)$$

$$[Co(OH)_3]^-_{(aq)} + [Fe(OH)_4]^-_{(aq)} \xrightarrow[180\ ^oC,4h]{\text{hydrothermal conditions}} CoFe_2O_{4\,(s)} + 4H_2O_{(\ell)} + 3OH^-_{(aq)} \quad (5)$$

Scheme 2 Proposed reaction mechanism of cobalt ferrite nanoparticles formation.

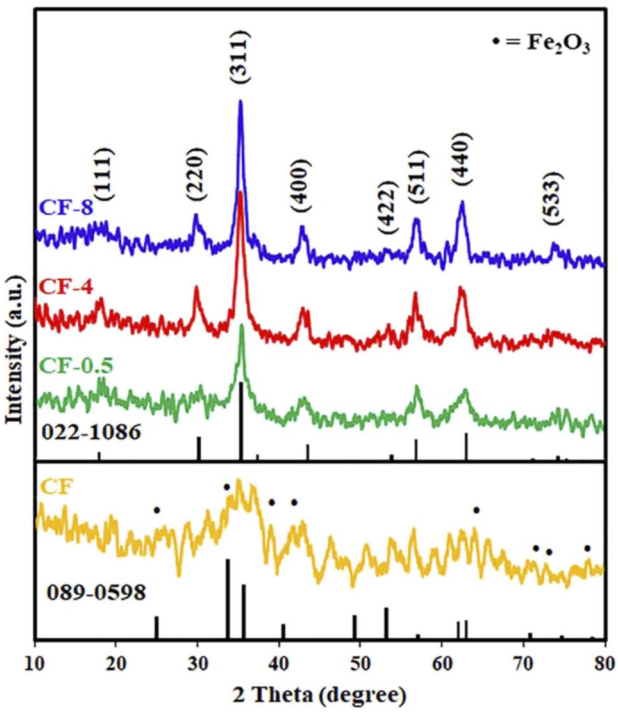

Fig. 1 XRD patterns of the prepared sample using co-precipitation method (CF), and the hydrothermal products: CF-0.5, CF-4, and CF-8, prepared at different reaction times: 0.5, 4, and 8 h, respectively.

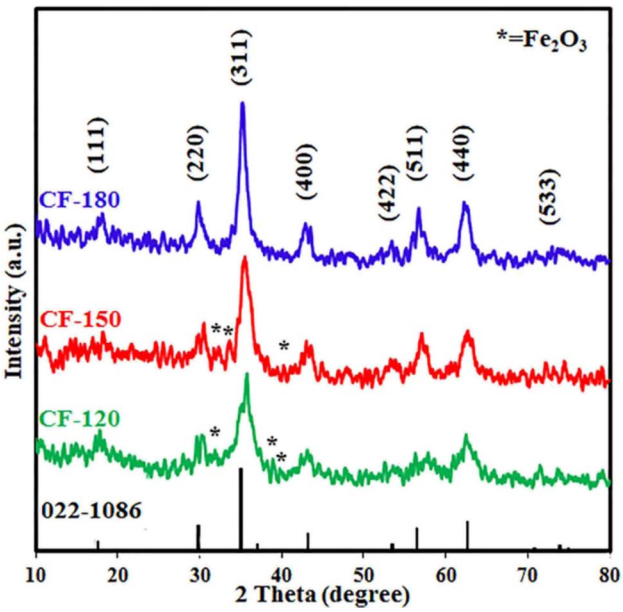

Fig. 2 XRD patterns of the hydrothermal products: CF-120, CF-150, and CF-180, prepared at different reaction temperatures: 120, 150, and 180 °C, respectively.

(D_{XRD}) of the prepared samples were estimated by using the Debye–Scherrer formula (1).[11,27,28]

$$D_{XRD} = K\lambda/\beta \cos\theta \quad (1)$$

where D_{XRD} stands for crystallite size (nm), K is a constant related to the shape of the crystal (=0.89), β is the full width of the diffraction line at the half-maximum intensity (FWHM) in radians, λ is the X-ray wavelength ($\lambda = 1.5406$ Å for Cu Kα), and θ refers to Bragg's angle of diffraction. It was observed that the lowest average crystallite size was found to be 3.6 nm for CF-0.5 sample while the largest average crystallite size was 8.5 nm for CF-8 sample. However, we have chosen the optimum hydrothermal reaction time to be 4 h since it gave CF-4 product with good crystallinity. Besides, this hydrothermal reaction time (4 h) saved time and energy as well as there is no significant difference between CF-4 and CF-8. The growth and nucleation of $CoFe_2O_4$ particles of can be attributed to the Ostwald ripening process. The Ostwald ripening process is the dissolution of small size particles which are redeposited into large size particles by passing time. This process may occur because smaller particles have higher surface energy and total Gibbs energy than larger particles, which are energetically undesirable.[29–34] Notably, our results are consistent with those reported in the literature.[31] For instance, Cabuil *et al.* found that the

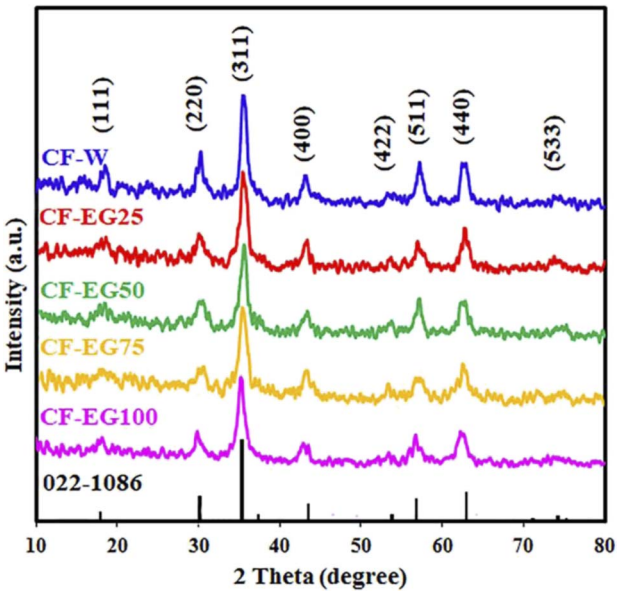

Fig. 3 XRD patterns of the hydrothermal products: CF-W, CF-EG25, CF-EG50, CF-EG75, and CF-EG100, prepared using different solvents: 100% water, 25% EG, 50% EG, 75% EG, and 100% EG (v/v), respectively.

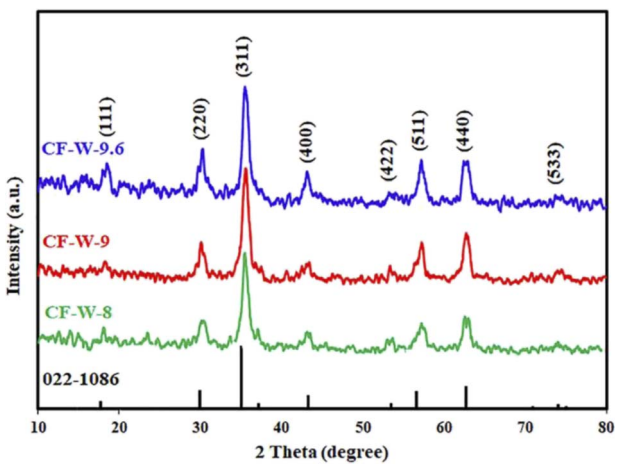

Fig. 4 XRD patterns of the hydrothermal products: CF-W-8, CF-W-9, and CF-W-9.6, prepared using different pH values: 8, 9, and 9.6, respectively.

mean size of the prepared $CoFe_2O_4$ NPs by the hydrothermal method was slightly larger than the mean diameter of the particles obtained with the usual co-precipitation method, which is probably due to the Ostwald ripening process.[31] Yang *et al.* prepared hollow anatase TiO_2 nanospheres *via* Ostwald ripening under hydrothermal conditions. They demonstrated the crystallinity of the products increased gradually with increasing the reaction time from 2 to 100 h.[34] Medeiros *et al.* concluded that the growth of crystallites of $CoFe_2O_4$ NPs by the hydrothermal method was enhanced by increasing the reaction time from 2 to 6 h.[32]

For comparison, we carried out the reaction of cobalt nitrate and iron nitrate in the presence of ammonium hydroxide using

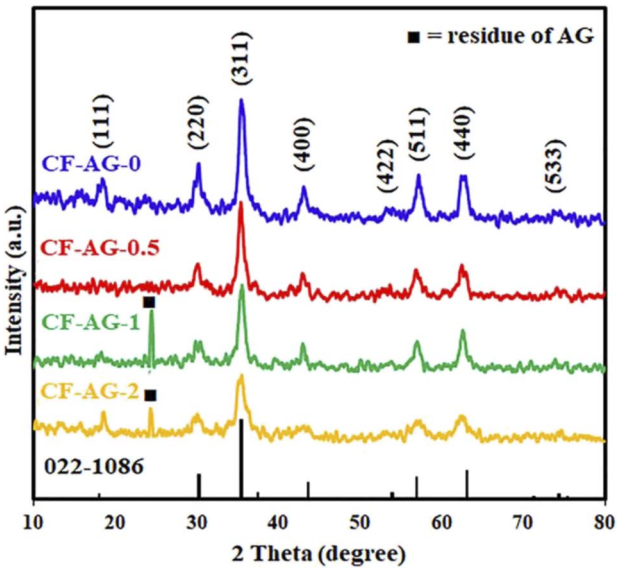

Fig. 5 XRD patterns of the hydrothermal products: CF-AG-0, CF-AG-0.5, CF-AG-1, and CF-AG-2 prepared using different amounts of AG: 0, 0.5, 1.0, and 2.0 g, respectively.

the usual co-precipitation method at 70 °C. However, the co-precipitation reaction did not produce pure cobalt ferrite nanoparticles and produced a semi-amorphous cubic cobalt ferrite (CF) with JCPDS card no. 022-1086 (ref. 26) along with other phases such as hematite with JCPDS card no. 089-0598,[35] as shown in Fig. 1. From the research that has been carried out, it is possible to conclude that the co-precipitation method was insufficient to give a pure cobalt ferrite phase while the hydrothermal procedure produced the desired $CoFe_2O_4$ product in single straightforward step without the need for a post thermal treatment.

3.1.3. Effect of temperature. The influence of the reaction temperature (120–180 °C) on the hydrothermal reaction of interest was studied. The XRD patterns of the products are displayed in Fig. 2. As shown in Fig. 2, the temperature of the hydrothermal process has a remarkable effect on the crystallinity and purity of the products. The data revealed that 180 °C reaction temperature produced pure cobalt ferrite product with an average crystallite size of 7.8 nm while decreasing the temperature influenced negatively the crystallinity and purity of the $CoFe_2O_4$ product. Lower reaction temperatures; 150 and 120 °C, generated $CoFe_2O_4$ products; CF-150 and CF-120, with lower crystallite sizes of 6.1 and 4.5 nm, respectively, along with other phases. Among these impurities was hematite (JCPDS card no. 15-0615)[36] and the corresponding diffraction peaks appeared at 2θ values of 31.9° (009), 33.9° (109), 38.8° (209), and 40.3° (316). Thus, the optimum reaction temperature for this hydrothermal treatment was selected to be 180 °C for the subsequent reactions. The high purity of the hydrothermally prepared cobalt ferrite product is probably owing to the precursors might be more reactive at higher temperatures and the lattice rearrangement was facilitated.[29] The obtained results are in good agreement with those reported by Abdulwahab *et al.* who reported on the synthesis of monodispersed iron cobalt oxide (Fe_2CoO_4) and iron manganese oxide ($Mn_{0.43}Fe_{2.57}O_4$) NPs using bimetallic

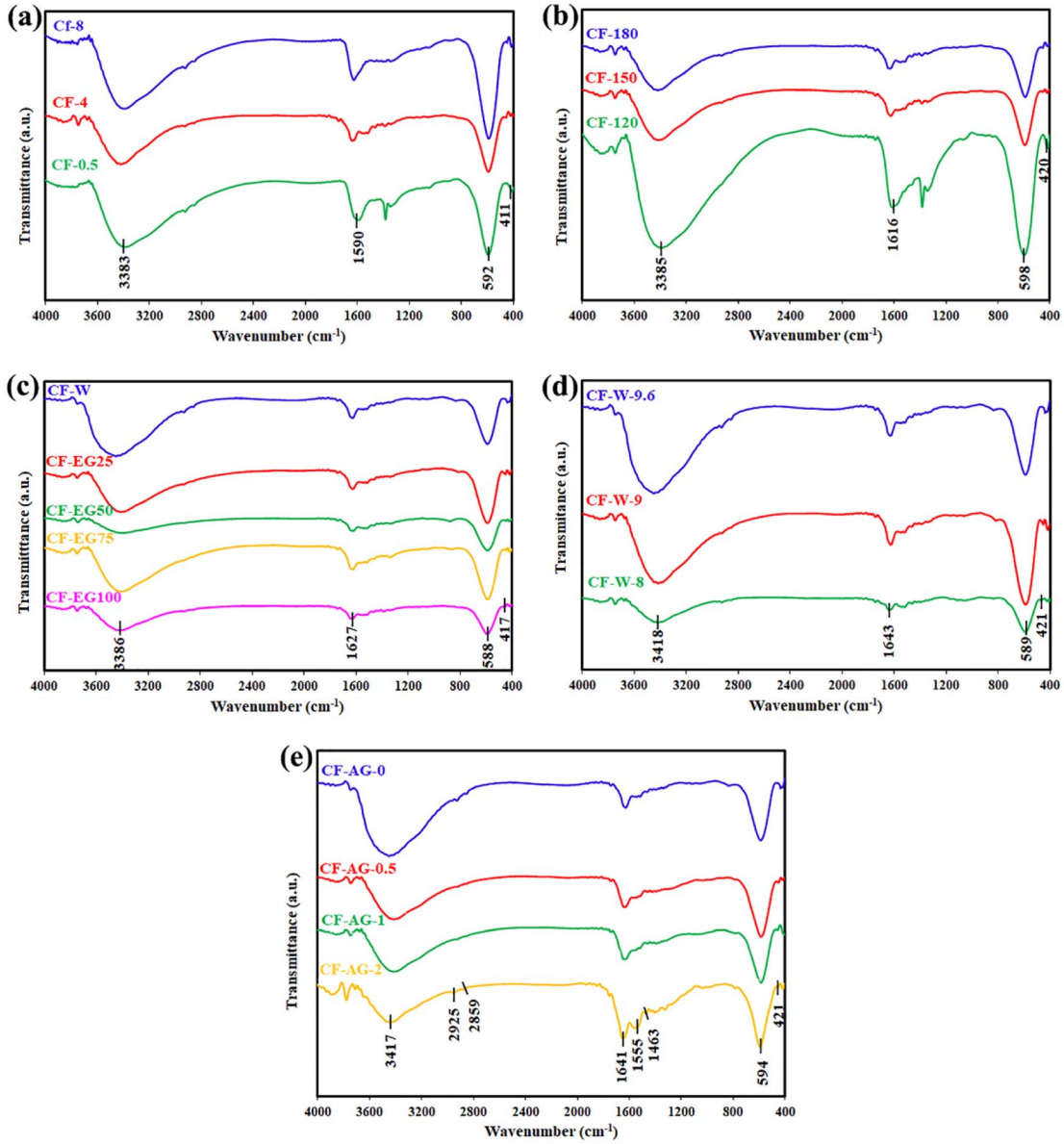

Fig. 6 FTIR spectra of the hydrothermally prepared samples at different parameters (a) time reaction (0.5, 4, and 8 h); (b) temperature reaction (120, 150, and 180 °C); (c) solvent (100% water, 25% EG, 50% EG, 75% EG, and 100% EG); (d) pH value (8, 9, and 9.6); and (e) Arabic gum amount (0, 0.5, 1, and 2 g).

pivalate clusters of $[Fe_2CoO(O_2CtBu)_6(HO_2CtBu)_3]$, $[Co_4Fe_2O_2(O_2CtBu)_{10}(MeCN)_2]$, and $[Fe_2MnO(O_2CtBu)_6(HO_2CtBu)_3]$, respectively, as single source precursors.[29]

3.1.4. Effect of solvent. The effect of solvent on the hydrothermal preparation of cobalt ferrite nanoparticles was also investigated. This was performed by carrying out the hydrothermal reactions in different solvents: ethylene glycol (EG), water (W), and mixtures of them (% EG (v/v)). The obtained XRD patterns are presented in Fig. 3. The XRD results revealed that the intensity of the diffraction peaks gradually enhanced as the ratio of ethylene glycol was reduced. The crystallite size of the products increased from 7.8 nm (for 100% ethylene glycol) to 12.9 nm (for 100% water). Based on these results, it could be concluded that the decrease of the crystallinity in the cobalt ferrite product when ethylene glycol (100%) was applied as a pure solvent might be attributed to the issue that ethylene glycol served as a capping agent during the growth of the product nuclei. Besides, ethylene glycol might form complexes with the metal ions of the utilized metal precursors which might restrict also the growth rate and formation of large crystallite-size products.[37] Additionally, the viscosity of water is lower than that of ethylene glycol. Consequently, the mobility of ions in water is higher which may bring about that the growth rate may exceed the nucleation rate, leading to the formation of larger cobalt ferrite particles in aqueous media.[38,39] We thus selected water solvent as the optimum solvent for this study due to the aforementioned reasons as well as it is the most environmentally friendly and inexpensive solvent compared to other solvents.[38] These results

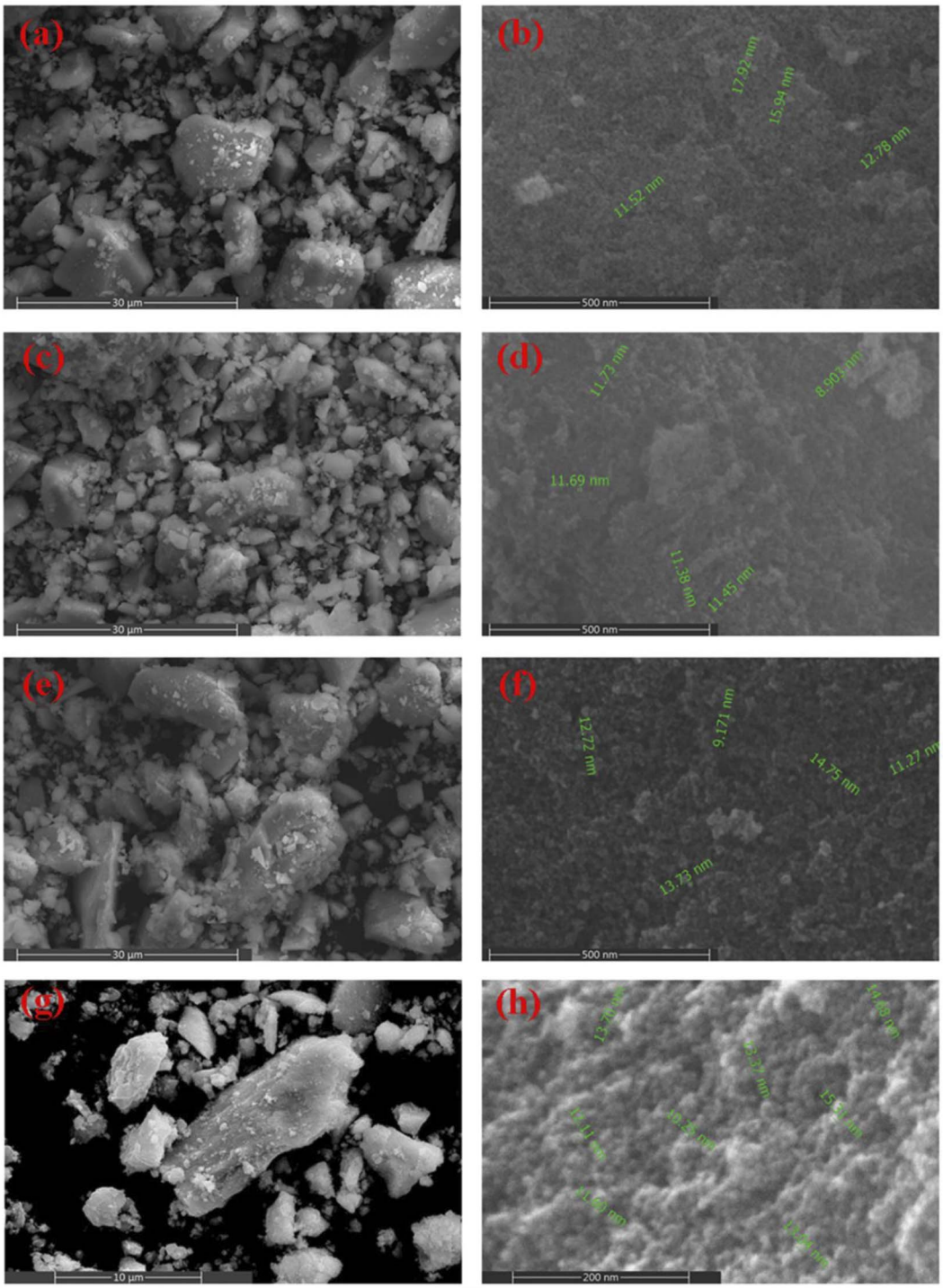

Fig. 7 FE-SEM images at different magnifications for CF-EG100 sample (a and b), CF-EG50 sample (c and d), CF-W sample (e and f), and CF-AG-0.5 sample (g and h).

are compatible with those reported by Mousavi Ghahfarokhi *et al.* They investigated the effect of ethylene glycol as a surfactant on the magnetic, structural, and optical properties of $SrFe_2O_4$ NPs using ethylene glycol with different weight percentages. They concluded that by increasing the weight percentages of the applied ethylene glycol, the intensity of diffraction peaks and consequently the crystallinity of the prepared samples was reduced.[37] Besides, Rishikeshi *et al.* studied the effects of the use of varying chain length glycols (ethylene glycol (EG), diethylene glycol (DEG), and polyethylene glycol 400 (PEG)) as solvents. The crystallite size for $ZnFe_2O_4$ products decreased by increasing the chain length of the used ethylene glycol derivatives. They also concluded that the degree of crystallinity of the zinc ferrite products may be related to the structure of the intermediately formed complex as well.[40]

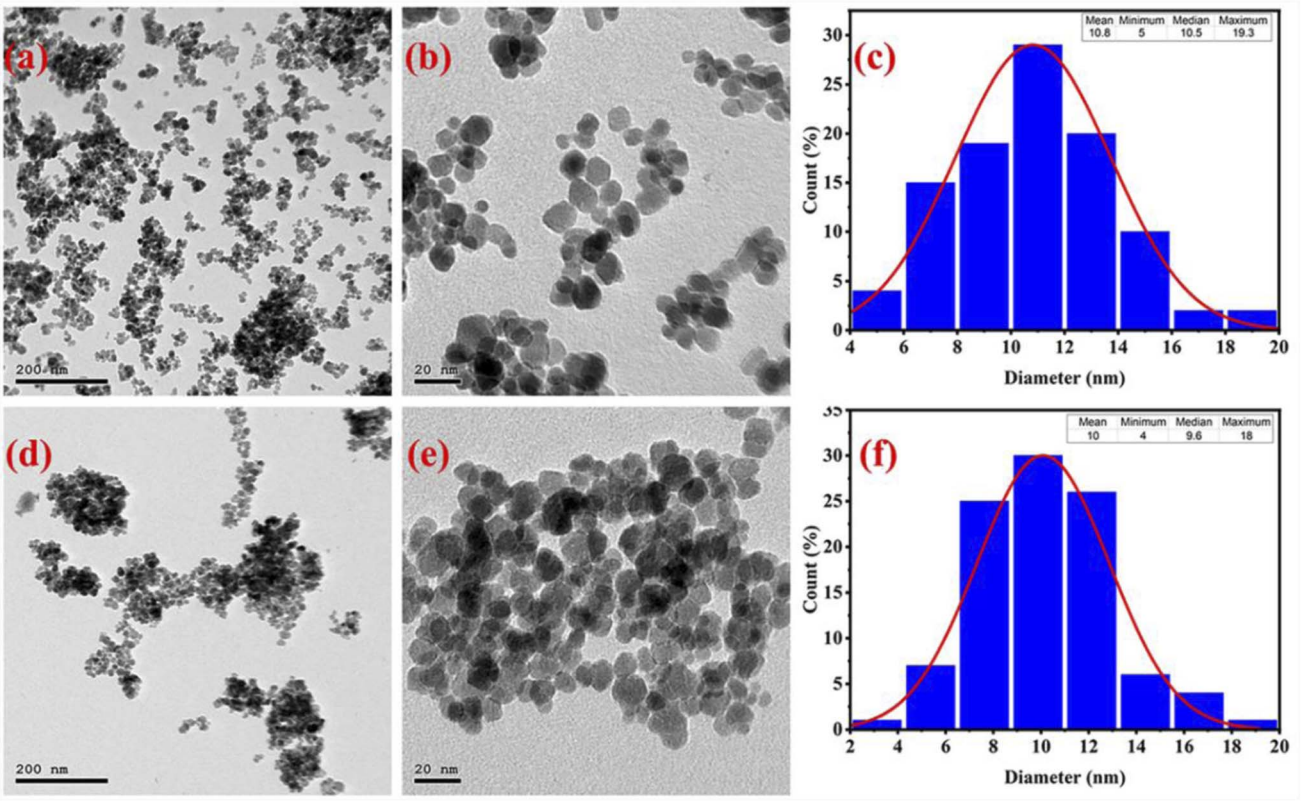

Fig. 8 HR-TEM images at different magnifications for CF-AG-0 sample (a and b), and CF-AG-0.5 sample (d and e). The size distribution histograms for CF-AG-0 (c) and CF-AG-0.5 (f) samples.

3.1.5. Effect of pH. The pH of the reaction medium was adjusted at different pH values (8, 9, and 9.6) by using the proper volume of ammonia solution 3 M. The XRD patterns of the products are depicted in Fig. 4. The results exhibited that the crystallinity of the products increased by increasing the pH value. The optimum pH value was chosen to be 9.6. These results can also be explained as follows. Cobalt ions $[Co(H_2O)_6]^{2+}$ precipitated by raising the pH values and the major precipitated molecules might be $Co(OH)_x^{2-x}$ which could be changed into more insoluble molecules ($Co(OH)_2$). In addition, cobalt salt has better solubility than iron salt, so cobalt ions require a higher pH value to precipitate.[32,41] The color of the supernatant after the hydrothermal reaction of prepared samples at 8 and 9 pH values was pale pink, evidence of the existence of the remaining cobalt, which was confirmed and detected by sodium hydroxide solution, leading to the formation of a blue precipitate. While at pH 9.6 value, the color of the supernatant was colorless, indicating the completion of the hydrothermal reaction. Similar results were reported by others.[32,41–44] For instance, Medeiros *et al.* investigated the influence of the pH factor on the crystallite size by means of the experimental design of $CoFe_2O_4$ NPs, which were prepared by the EDTA/citrate complexing method and the hydrothermal method. They indicated that the enhancement of the crystallinity of the products may be related to the hydrolysis step dependent on pH value. Where in the presence of excess sodium hydroxide (*i.e.* high pH), the formed cobalt hydroxide is surrounded by a large number of hydroxyl groups, leading to the production of large particles.[32] Giri *et al.* optimized the pH parameter for the preparation of $Co_{1-x}Zn_xFe_2O_4$, ($0 \leq x \leq 0.8$) NPs by the microwave refluxing method and concluded that the crystallinity of prepared samples increased with rising pH value.[43] Safi *et al.* synthesized cobalt ferrite nanoparticles by the co-precipitation method at different pH values. The XRD analysis of the products indicated that the prepared samples at higher pH values were pure $CoFe_2O_4$ phase, while the samples prepared at lower pH values showed α-Fe_2O_3 phase in addition to the $CoFe_2O_4$ phase.[41]

3.1.6. Effect of using Arabic gum (AG) as surfactant. We investigated the influence of the presence of different amounts of Arabic gum as surfactant on the hydrothermal preparation of cobalt ferrite under the previously obtained optimum conditions. The XRD patterns of the obtained products are presented in Fig. 5. The results exhibited that on increasing the amount of AG in the hydrothermal treatment of interest the diffraction peaks of $CoFe_2O_4$ tend to be broader and the crystallite size gets lower. This is probably due to serving the AG agent as a surfactant in this reaction. Besides, cobalt hydroxide and ferric hydroxide can intercalate with the positive groups of AG and create ion pairs through electrostatic interactions that reduce the surface energy and surface tension of coated cobalt ferrite nanoparticles. Accordingly, the nucleation energy barrier decreased, and the nucleation rate became faster. As a result, uniform growth occurred and gave a narrow-size

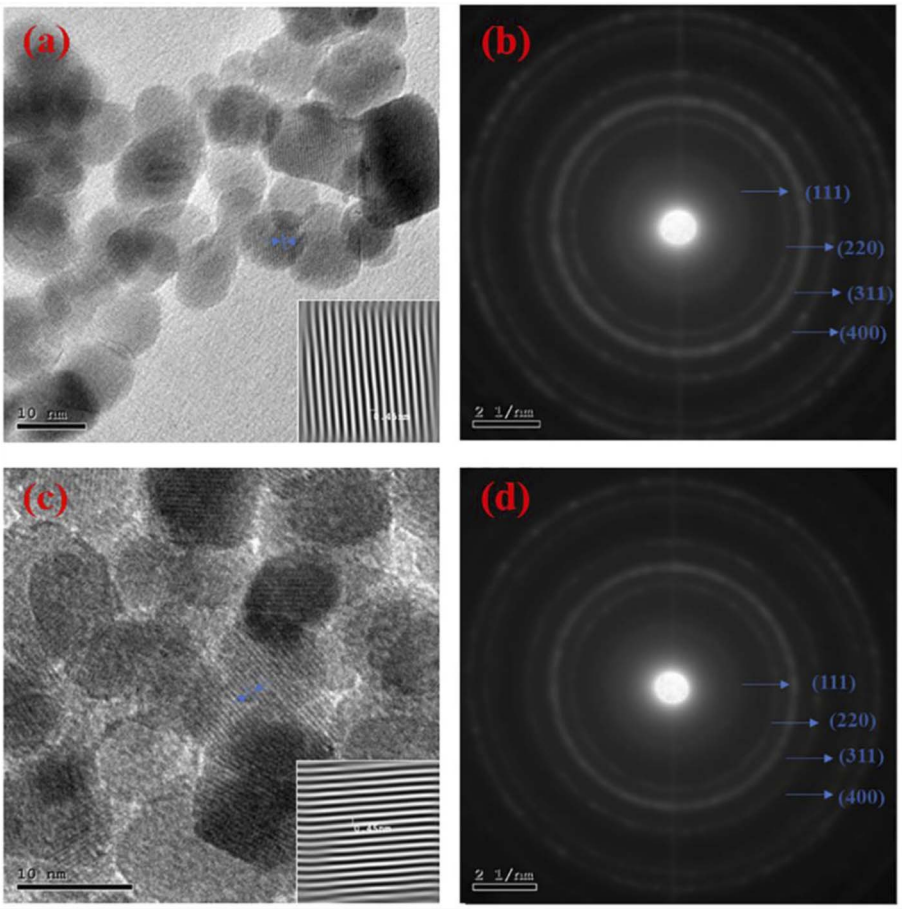

Fig. 9 HR-TEM images at high magnifications for CF-AG-0 sample (a); the inset presents the interplanar space for CF-AG-0 sample, and (c) CF-AG-0.5 sample; the inset is the interplanar space for CF-AG-0.5 sample. SAED patterns for CF-AG-0 sample (b), and (d) CF-AG-0.5 sample.

distribution.[45,46] By inspection of XRD patterns, there is an additional XRD diffraction peak appeared at the 2-theta position (24.4°) for the samples prepared using >0.5 g of Arabic gum due to the residue of Arabic gum. Therefore, the appropriate amount of arabic gum was chosen to be 0.5 g for the present hydrothermal preparation. Other research groups reported a similar trend as follows. Akbari *et al.* studied the influence of polyvinyl alcohol (PVA) on the characteristics of cobalt ferrite NPs prepared by the co-precipitation method and followed by calcination at 700 °C. By adding PVA, the peaks of XRD became broader, and the estimated crystallite sizes of the prepared samples were reduced by increasing the amount of polyvinyl alcohol.[45] Amanda *et al.* presented a hydrothermal route for the preparation of different metal ferrites using various types of surfactants. They demonstrated that varying the surfactant had a significant impact on the shape and particle size of the generated $CoFe_2O_4$ NPs.[46] Besides, Ansari *et al.* prepared tunable $CoFe_2O_4$ nanoparticles using an oleic acid-based solvothermal method. By increasing the oleic acid concentration, the average crystallite size was reduced.[47]

3.2 The reaction mechanism

The mechanism of the hydrothermal formation of cobalt ferrite can be explained based on the dissolution, nucleation, and growth process mechanism (Scheme 2). These reactions can proceed as follows: (1) dissolution of cobalt and ferric nitrate salts according to eqn (1) and (2) (Scheme 2). Afterward, cobalt and iron aqua complexes underwent hydrolysis in the presence of ammonium hydroxide solution, forming cobalt and ferric hydroxides based on eqn (3) and (4) (Scheme 2). Finally, under hydrothermal conditions, cobalt and ferric hydroxides may undergo dehydration followed by the growth of cobalt ferrite (eqn (5), Scheme 2).[48]

3.3 Fourier transform infrared investigation (FT-IR)

We investigated the hydrothermally prepared products by using FT-IR spectroscopy to identify their chemical composition and functional groups, as displayed in Fig. 6. The FT-IR spectra of all samples showed two bands at *ca.* 416 and 590 cm^{-1}, owing to the vibrational frequencies of Co–O bonds in octahedral sites and Fe–O bonds in tetrahedral sites, respectively, suggesting the formation of the cobalt ferrite NPs phase.[49–51] In addition, the bands appeared at *ca.* 3385 and 1616 cm^{-1} are related to O–H stretching vibration and H–O–H bending vibration, respectively, originating from moisture and residue of ethylene glycol and Arabic gum.[14,43,52,53] Notably, the broad band at *ca.* 3385 cm^{-1} is probably due to overlapped O–H and N–H stretching vibrations.[54] However, Fig. 6(e) exhibited vibrational

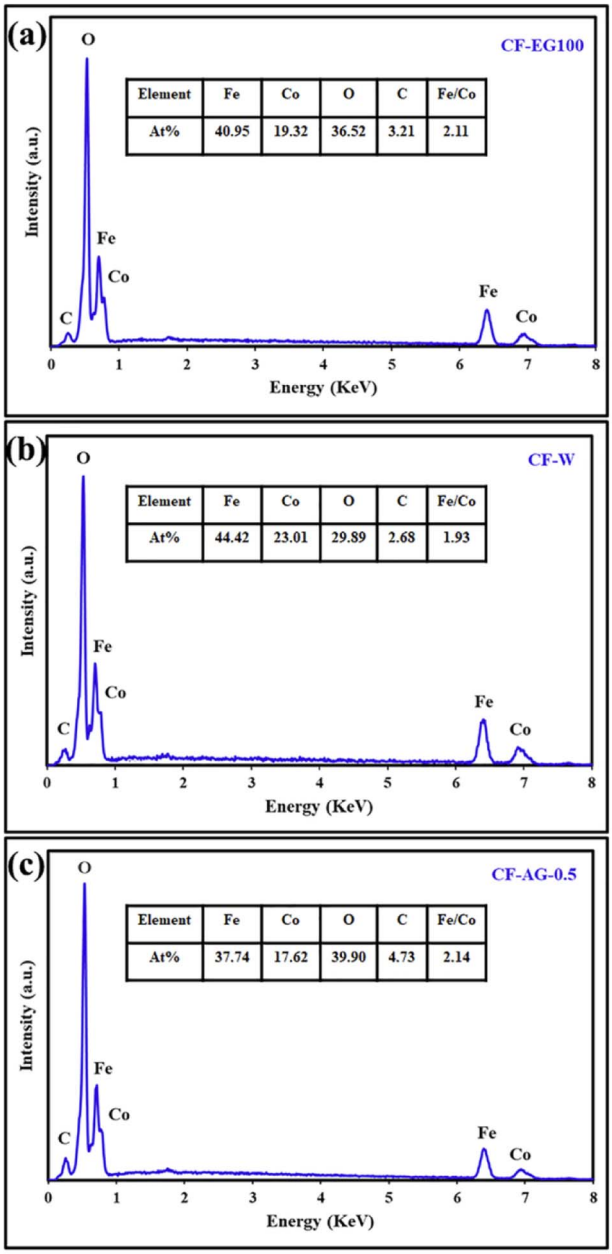

Fig. 10 EDS spectra of the CF-EG100 sample (a), CF-W sample (b), and CF-AG-0.5 sample (c).

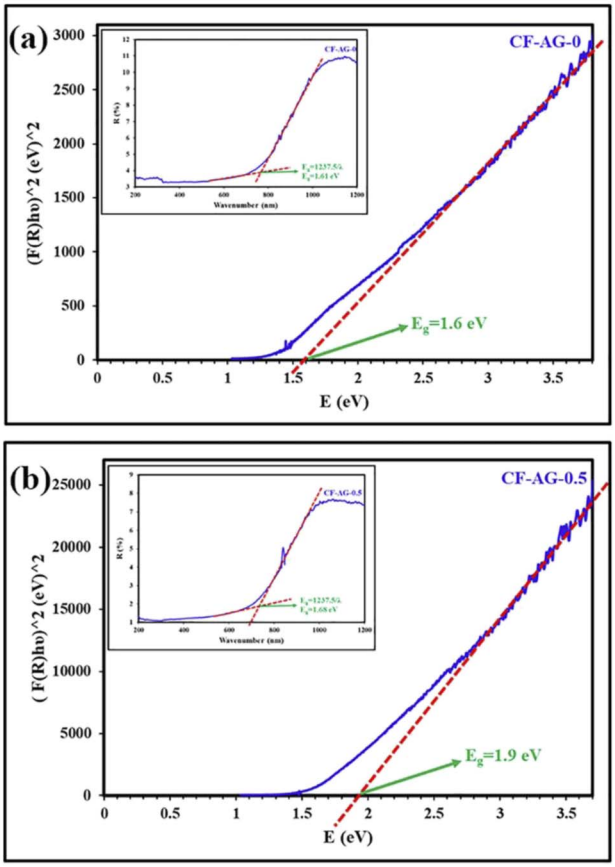

Fig. 11 Tauc plot for CF-AG-0 sample (a), and CF-AG-0.5 sample (b); the insets of (a) and (b) are the UV-visible diffuse reflectance spectra (DRS) for CF-AG-0 and CF-AG-0.5 samples, respectively.

bands at *ca.* 2925 and 2859 cm^{-1} which might be attributed to asymmetric and symmetric stretching vibrations, respectively, of the CH_2 groups of the organic residue of Arabic gum.[20,43,55] This figure also showed stretching vibration of C=O (*ca.*1743 cm^{-1}),[56,57] bands of asymmetric and symmetric stretching vibrations of the COO^- (*ca.* 1555 and 1517 cm^{-1}, respectively),[20,58] and bending vibration of H–C–H (*ca.* 1463 cm^{-1})[43] of the used excess Arabic gum in the hydrothermal treatment of interest.

3.4 The morphology

The morphological characteristics of cobalt ferrite nanoparticles were examined by FE-SEM, HR-TEM, and selected area electron diffraction (SAED) techniques. The particle size of $CoFe_2O_4$ NPs was calculated using the corresponding size distribution histograms. Fig. 7(a–h) displays the FE-SEM images of CF-EG100, CF-EG50, CF-W, and CF-AG-0.5 samples at different magnifications. The FE-SEM images of the samples showed spherical agglomerated particles of sizes below 15 nm. This agglomeration is due to the magnetic interaction and van der Waals forces between the nanoparticles.[11,59,60] On the other hand, the HR-TEM images and the corresponding size distribution histograms were obtained for CF-AG-0 and CF-AG-0.5 samples and displayed in Fig. 8(a–f). The TEM images of both samples revealed that most particles are spherical in shape, but there are also some irregular shaped particles. The mean particle size was determined by calculating the diameter of 100 particles from several recorded images using Image j software and representing them in a histogram with normal distribution by the origin 2022 program. According to Sturges' criteria, the total number of bins (k) is calculated from this relation $k = 1 + 3.322 \log(N)$, where N is the total number of recorded particles and the bin width (W) is equal to $W = (D_{max} - D_{min})/k$.[61] The mean particle size was found to be *ca.* 10.8 and 10 nm for the CF-AG-0 and CF-AG-0.5 nanoparticles, respectively. These values are close to the crystallite size (D_{XRD}) values calculated from the XRD data. However, the disparity between the particle size values calculated by the two approaches could be attributed

to only the largest particles are recorded in XRD, while in TEM, the size distribution with an average diameter is determined for a small number of particles.[50] Other research groups reported similar and different morphologies of $CoFe_2O_4$ nanoparticles. Gandhi *et al.* prepared spherical cobalt ferrite nanoparticles by co-precipitation method for magnetic hyperthermia,[62] while Ratkovski *et al.* produced hexagonal cobalt ferrite nanoparticles by co-precipitation method for sensing phosphate ions in aqueous media and biological samples.[63]

In addition, the interplanar spacing was detected and presented in the insets of Fig. 9(a–c), which equaled 0.46 and 0.45 nm for CF-AG-0 and CF-AG-0.5, respectively. The corresponding SAED patterns are shown in Fig. 9(b–d) which display sharp and discrete rings can well be indexed to (111), (220), (311) and (400) planes (JCPDS card no. 022-1086)[26] for both samples. These results indicated a pure, crystalline spinel cubic structure of cobalt ferrite, which agreed well with the XRD results.

3.5 Energy-dispersive X-ray spectroscopy (EDS) analysis

EDS analysis was performed for CF-EG100, CF-W, and CF-AG-0.5 samples as depicted in Fig. 10 (a–c). The obtained data confirmed the successful preparation of cobalt ferrite since the samples contain only iron, cobalt, and oxygen elements in addition to traces of carbon element as impurities. The presence of carbon may be due to various factors, including the residue from ethylene glycol, arabic gum, or connection with any organic contaminants during the sample preparation for the EDS analysis. The Fe/Co molar ratios for the CF-EG100, CF-W, and CF-AG-0.5 were found to be 2.11, 1.93, and 2.14, respectively, as presented in the inset tables in Fig. 10, and these values are consistent with the corresponding theoretical molar ratios.

3.6 The optical properties

The optical properties and band gap values for CF-AG-0 and CF-AG-0.5 samples were estimated by using UV-visible diffuse reflectance spectroscopy (DRS), Fig. 11. The diffuse reflectance spectroscopy (DRS) is a reliable technique for estimation of the band gap energy because this technique does not require special treatment for the samples.[64–66] The absorption profile is influenced by various factors such as synthetic method, lattice parameters, surface roughness, band gap, and impurity centers.[67] As depicted in the inset of Fig. 11, both CF-AG-0 and CF-AG-0.5 samples exhibited nearly the same absorption behavior with only one absorption edge in the visible region at wavelength of 765 and 735 nm, respectively. The optical band gap energy (E_g) can be determined by using the following relationship (2).[68] The estimated band gap values for CF-AG_0 and CF-$AG_{0.5}$ samples are 1.61 and 1.68 eV, respectively.

$$E_g = \frac{1237.5}{\lambda} \quad (2)$$

where λ is the wavelength of the absorption edge, which is determined by the intercept on the wavelength axis as shown in the inset of Fig. 11.

Besides, the band gap energy is also calculated by the Tauc method by using eqn (3).[69,70]

$$\alpha h\nu = A(h\nu - E_g)^n \quad (3)$$

where α, h, ν, A and n are absorption coefficient, Planck's constant, light frequency, proportionality constant, and the nature of optical transitions either direct allowed transitions ($n = \frac{1}{2}$) or indirect allowed transitions ($n = 2$), respectively. In the literature, the kind of electronic transition for ferrite materials is not completely agreed, but it is clear that the direct allowed transition is more suitable for these materials.[69–72] The Schuster–Kubelka–Munk (SKM) function was applied to convert the reflectance data into the remission function $F(R_\infty)$, which gives the ratio between the absorption coefficient (K) and scattering coefficient (S) as seen in eqn (4).[69] Eqn (3) can be written as eqn (5) after substitution $a = F(R)$ and $n = 2$.

$$F(R) = \alpha = \frac{K}{S} = \frac{(1-R)^2}{2R} \quad (4)$$

$$(F(R)h\nu)^2 = A(h\nu - E_g) \quad (5)$$

Through a plot of $(F(R)h\nu)^2$ *versus* $E = h\nu$, the band gap can be derived by extrapolating the linear section representing the absorption onset of the curve to intercept the energy axis at $(F(R)h\nu)^2 =$ zero. The measured band gap values are 1.6 and 1.9 eV for CF-AG-0 (D_{XRD} = 12.9 nm) and CF-AG-0.5 (D_{XRD} = 12.4 nm), respectively. The band gap values increase as the crystallite size of the samples decreases, and these band gap values are greater than reported theoretical values for bulk cobalt ferrite (0.8 eV, 0.72 eV, and 0.63 eV).[73] This may be illustrated by the quantum confinement regime at nanoscale. Quantum confinement is an important phenomenon for semiconductor nanomaterials where electron and hole carriers are closer together at the nanoscale, enhancing interaction between them and confining them in a very narrow region, so more energy is required to separate them. As described in eqn (6), the shift in bulk band gap energy increases with size approximately to or less than the bulk exciton-Bohr radius.[68,71]

$$E_{sh} = \frac{\hbar^2\pi^2}{2R^2}\left[\frac{1}{m_e} + \frac{1}{m_h}\right] - \frac{1.8e^2}{\varepsilon_1 R} + \frac{e^2}{R}\left\langle \sum_{n=1}^{\infty} a_n \left(\frac{\vec{S}}{R}\right)^{2n} \right\rangle \quad (6)$$

where E_{sh} is the shift from bulk band gap energy, R is the crystallite radius, m_h and m_e are defined as the effective masses of the hole and electron carriers, respectively, $\vec{S}$ represents the position vector corresponding to the effective charge distribution of the system, and a_n is a quantity that is based on ε_1 and ε_2, where ε_1 and ε_2 are the dielectric coefficient of the material and surrounding medium, respectively. In the literature review, Andhare *et al.* demonstrated the influence of Zn doping on optical, structural, and magnetic properties of cobalt ferrite nanoparticles, which were synthesized by the co-precipitation method. The estimated optical band gap using the Tauc plot decreased from 2.831 eV to 2.258 eV related to increasing particle size from 12 nm to 17 nm with increasing Zn amount in $Co_{1-x}Zn_xFe_2O_4$ where $x = 0.0, 0.3, 0.5, 0.7$, and 1.0. Additionally,

Singh *et al.* studied the size-dependent behavior of $CoFe_2O_4$ NPs using synchrotron radiation-based techniques. For the optical behavior, the estimated optical band gaps were 1.90 ± 0.02, 1.85 ± 0.02, 1.80 ± 0.02, and 1.69 ± 0.02 eV for the annealed samples at 300, 500, 700, and 900 °C, respectively. It is clear that the band gap energy decreases with increasing the crystallite size. This observation may be attributed to the brass model.[68,71]

4. Conclusions

In summary, tunable-size, pure, spherical cobalt ferrite nanoparticles were successfully synthesized by a facile, eco-friendly hydrothermal route within four hours using cobalt nitrate, ferric nitrate, ammonium hydroxide, and arabic gum. In this regard, we controlled the products' composition and crystallinity by changing the reaction conditions such as the reaction time (0.5–8 h), reaction temperature (120–180 °C), percentage of ethylene glycol (0–100% (v/v)), pH value (8–9.6), and amount of Arabic gum (0–2 g). The results exhibited that the crystallite size was enhanced from 3.6 to 8.5 nm by increasing the reaction time from 0.5 to 8 h; from 4.5 to 7.8 nm by raising the reaction temperature from 120 to 180 °C; and from 12.3 to 12.9 nm by increasing the pH value from 8 to 9.6, respectively. Whereas it was reduced from 12.9 to 7.8 nm by increasing the percentage of EG in aqueous solutions from 0% to 100% (v/v) and from 12.4 to 11.1 nm by increasing AG amount from 0 to 2 g, respectively. Based on the results, it could be deduced that the optimal hydrothermal treatment was carried out at 180 °C and pH 9.6 for 4 h in aqueous solutions. On the other hand, performing the same reaction using the usual co-precipitation method gave a semi-amorphous cobalt ferrite product along with other impurities such as hematite. The as-synthesized products were characterized by using XRD, FT-IR, EDS, DRS, FE-SEM, HR-TEM, and SAED techniques. The SAED patterns confirmed the formation of highly pure and crystalline spinel structure of $CoFe_2O_4$, which was consistent with the XRD results. The estimated optical band gap energy was in the range of 1.6–1.9 eV, indicating the semiconducting characteristics of the prepared cobalt ferrite nanoparticles. In addition, the results indicated that the developed hydrothermal procedure is a good candidate for the preparation of various metal ferrites in suitable crystallite sizes from aqueous solutions.

Conflicts of interest

There are no conflicts to declare.

Acknowledgements

We would like to express our appreciation and gratitude to Benha University and Zagazig University, Egypt for their support for this work.

References

1 X. Xie, B. Wang, Y. Wang, C. Ni, X. Sun and W. Du, Spinel structured MFe2O4 (M = Fe, Co, Ni, Mn, Zn) and their composites for microwave absorption: a review, *Chem. Eng. J.*, 2022, **428**, 131160.
2 K. Malaie and M. R. Ganjali, Spinel nano-ferrites for aqueous supercapacitors; linking abundant resources and low-cost processes for sustainable energy storage, *J. Energy Storage*, 2021, **33**, 102097.
3 N. Chaibakhsh and Z. Moradi-Shoeili, Enzyme mimetic activities of spinel substituted nanoferrites (MFe2O4): a review of synthesis, mechanism and potential applications, *Mater. Sci. Eng. C*, 2019, **99**, 1424–1447.
4 R. Tandon, N. Tandon and S. M. Patil, Overview on magnetically recyclable ferrite nanoparticles: synthesis and their applications in coupling and multicomponent reactions, *RSC Adv.*, 2021, **11**, 29333–29353.
5 Q. Zhao, Z. Yan, C. Chen and J. Chen, Spinels: Controlled Preparation, Oxygen Reduction/Evolution Reaction Application, and Beyond, *Chem. Rev.*, 2017, **117**, 10121–10211.
6 A. Goyal, S. Bansal and S. Singhal, Facile reduction of nitrophenols: comparative catalytic efficiency of MFe2O4 (M = Ni, Cu, Zn) nano ferrites, *Int. J. Hydrogen Energy*, 2014, **39**, 4895–4908.
7 S. G. Kakade, R. C. Kambale, Y. D. Kolekar and C. V. Ramana, Dielectric, electrical transport and magnetic properties of Er3+ substituted nanocrystalline cobalt ferrite, *J. Phys. Chem. Solids*, 2016, **98**, 20–27.
8 T. Amrillah, A. Hermawan, Y. Bitla, M. A. Baqiya, L. T. Quynh, A. Taufik, S. Yin and J.-Y. Juang, Preferentially Oriented Nanometer-Sized CoFe2O4 Mesocrystals Embedded in the BiFeO3 Matrix for Opto-Magnetic Device Applications, *ACS Appl. Nano Mater.*, 2021, **4**, 11249–11259.
9 V. V. Jadhav, S. D. Shirsat, U. B. Tumberphale and R. S. Mane, in *Spinel Ferrite Nanostructures for Energy Storage Devices*, ed. R. S. Mane and V. V. Jadhav, Elsevier, 2020, ch. 3 – Properties of Ferrites, pp. 35–50.
10 T. N. Pham, T. Q. Huy and A.-T. Le, Spinel ferrite (AFe2O4)-based heterostructured designs for lithium-ion battery, environmental monitoring, and biomedical applications, *RSC Adv.*, 2020, **10**, 31622–31661.
11 Shyamaldas, M. Bououdina and C. Manoharan, Dependence of structure/morphology on electrical/magnetic properties of hydrothermally synthesised cobalt ferrite nanoparticles, *J. Magn. Magn. Mater.*, 2020, **493**, 165703.
12 X. Guoxi and X. Yuebin, Effects on magnetic properties of different metal ions substitution cobalt ferrites synthesis by sol–gel auto-combustion route using used batteries, *Mater. Lett.*, 2016, **164**, 444–448.
13 D. H. K. Reddy and Y.-S. Yun, Spinel ferrite magnetic adsorbents: alternative future materials for water purification?, *Coord. Chem. Rev.*, 2016, **315**, 90–111.
14 M. Y. Nassar and M. Khatab, Cobalt ferrite nanoparticles via a template-free hydrothermal route as an efficient nano-adsorbent for potential textile dye removal, *RSC Adv.*, 2016, **6**, 79688–79705.
15 L. Hu, M. Li, L. Cheng, B. Jiang and J. Ai, Solvothermal synthesis of octahedral and magnetic CoFe2O4–reduced graphene oxide hybrids and their photo-Fenton-like

behavior under visible-light irradiation, *RSC Adv.*, 2021, **11**, 22250–22263.

16 S. Y. Srinivasan, K. M. Paknikar, D. Bodas and V. Gajbhiye, Applications of cobalt ferrite nanoparticles in biomedical nanotechnology, *Nanomedicine*, 2018, **13**, 1221–1238.

17 B. Debnath, H. G. Salunke and S. Bhattacharyya, Spin Disorder and Particle Size Effects in Cobalt Ferrite Nanoparticles with Unidirectional Anisotropy and Permanent Magnet-like Characteristics, *J. Phys. Chem. C*, 2020, **124**, 25992–26000.

18 E. P. Muniz, L. S. D. de Assunção, L. M. de Souza, J. J. K. Ribeiro, W. P. Marques, R. D. Pereira, P. S. S. Porto, J. R. C. Proveti and E. C. Passamani, On cobalt ferrite production by sol-gel from orange fruit residue by three related procedures and its application in oil removal, *J. Clean. Prod.*, 2020, **265**, 121712.

19 S. M. Ansari, K. C. Ghosh, R. S. Devan, D. Sen, P. U. Sastry, Y. D. Kolekar and C. V. Ramana, Eco-Friendly Synthesis, Crystal Chemistry, and Magnetic Properties of Manganese-Substituted CoFe2O4 Nanoparticles, *ACS Omega*, 2020, **5**, 19315–19330.

20 A. Chaudhuri and K. Mandal, Dynamic magnetic properties of monodisperse CoFe2O4 nanoparticles synthesized by a facile solvothermal technique, *Phys. B*, 2019, **575**, 311640.

21 M. Y. Nassar, M. M. Moustafa and M. M. Taha, Hydrothermal tuning of the morphology and particle size of hydrozincite nanoparticles using different counterions to produce nanosized ZnO as an efficient adsorbent for textile dye removal, *RSC Adv.*, 2016, **6**, 42180–42195.

22 M. Bastianello, S. Gross and M. T. Elm, Thermal stability, electrochemical and structural characterization of hydrothermally synthesised cobalt ferrite (CoFe2O4), *RSC Adv.*, 2019, **9**, 33282–33289.

23 Z. Gu, X. Xiang, G. Fan and F. Li, Facile Synthesis and Characterization of Cobalt Ferrite Nanocrystals via a Simple Reduction–Oxidation Route, *J. Phys. Chem. C*, 2008, **112**, 18459–18466.

24 G. B. Ji, S. L. Tang, S. K. Ren, F. M. Zhang, B. X. Gu and Y. W. Du, Simplified synthesis of single-crystalline magnetic CoFe2O4 nanorods by a surfactant-assisted hydrothermal process, *J. Cryst. Growth*, 2004, **270**, 156–161.

25 P. C. R. Varma, R. S. Manna, D. Banerjee, M. R. Varma, K. G. Suresh and A. K. Nigam, Magnetic properties of CoFe2O4 synthesized by solid state, citrate precursor and polymerized complex methods: a comparative study, *J. Alloys Compd.*, 2008, **453**, 298–303.

26 P. A. Asogekar, S. K. Gaonkar, A. Kumar and V. M. S. Verenkar, Influence of Co over magnetically benign Zn ferrite system and study of its structural, dielectric, superparamagnetic and antibacterial efficacy, *Mater. Res. Bull.*, 2021, **141**, 111330.

27 M. Y. Nassar, I. S. Ahmed and H. S. Hendy, A facile one-pot hydrothermal synthesis of hematite (α-Fe2O3) nanostructures and cephalexin antibiotic sorptive removal from polluted aqueous media, *J. Mol. Liq.*, 2018, **271**, 844–856.

28 R. Jenkins and R. L. Snyder, Instruments for the Measurement of Powder Patterns, in *Introduction to X-ray Powder Diffractometry*, John Wiley & Sons, Inc., 1996, pp. 173–203.

29 K. O. Abdulwahab, M. A. Malik, P. O'Brien, G. A. Timco, F. Tuna, C. A. Muryn, R. E. P. Winpenny, R. A. D. Pattrick, V. S. Coker and E. Arenholz, A One-Pot Synthesis of Monodispersed Iron Cobalt Oxide and Iron Manganese Oxide Nanoparticles from Bimetallic Pivalate Clusters, *Chem. Mater.*, 2014, **26**, 999–1013.

30 J. V. Alemán, A. V. Chadwick, J. He, M. Hess, K. Horie, R. G. Jones, P. Kratochvíl, I. Meisel, I. Mita, G. Moad, S. Penczek and R. F. T. Stepto, Definitions of terms relating to the structure and processing of sols, gels, networks, and inorganic-organic hybrid materials (IUPAC Recommendations 2007), *Pure Appl. Chem.*, 2007, **79**, 1801–1829.

31 V. Cabuil, V. Dupuis, D. Talbot and S. Neveu, Ionic magnetic fluid based on cobalt ferrite nanoparticles: influence of hydrothermal treatment on the nanoparticle size, *J. Magn. Magn. Mater.*, 2011, **323**, 1238–1241.

32 I. A. F. de Medeiros, A. L. Lopes-Moriyama and C. P. de Souza, Effect of synthesis parameters on the size of cobalt ferrite crystallite, *Ceram. Int.*, 2017, **43**, 3962–3969.

33 B. Liu and X. Hu, in *Advanced Nanomaterials for Pollutant Sensing and Environmental Catalysis*, ed. Q. Zhao, Elsevier, 2020, ch. 1 – Hollow Micro- and Nanomaterials: Synthesis and Applications, pp. 1–38.

34 H. G. Yang and H. C. Zeng, Preparation of Hollow Anatase TiO2 Nanospheres via Ostwald Ripening, *J. Phys. Chem. B*, 2004, **108**, 3492–3495.

35 V. A. Sadykov, L. A. Isupova, S. V. Tsybulya, S. V. Cherepanova, G. S. Litvak, E. B. Burgina, G. N. Kustova, V. N. Kolomiichuk, V. P. Ivanov, E. A. Paukshtis, A. V. Golovin and E. G. Avvakumov, Effect of Mechanical Activation on the Real Structure and Reactivity of Iron (III) Oxide with Corundum-Type Structure, *J. Solid State Chem.*, 1996, **123**, 191–202.

36 B. Schrader, *Z. fur Anorg. Allg. Chem.*, 1963, **320**, 205.

37 S. E. M. Ghahfarokhi and E. M. Shobegar, An investigation of the ethylene glycol surfactant on the structural, microstructure, magnetic and optical properties of SrFe2O4 nanoparticles, *J. Magn. Magn. Mater.*, 2020, **495**, 165866.

38 S. H. Feng and G. H. Li, in *Modern Inorganic Synthetic Chemistry*, ed. R. Xu and Y. Xu, Elsevier, Amsterdam, 2nd edn, 2017, ch. 4 – Hydrothermal and Solvothermal Syntheses, pp. 73–104.

39 V. Georgiadou, V. Tangoulis, I. Arvanitidis, O. Kalogirou and C. Dendrinou-Samara, Unveiling the Physicochemical Features of CoFe2O4 Nanoparticles Synthesized via a Variant Hydrothermal Method: NMR Relaxometric Properties, *J. Phys. Chem. C*, 2015, **119**, 8336–8348.

40 S. N. Rishikeshi, S. S. Joshi, M. K. Temgire and J. R. Bellare, Chain length dependence of polyol synthesis of zinc ferrite nanoparticles: why is diethylene glycol so different?, *Dalton Trans.*, 2013, **42**, 5430–5438.

41 R. Safi, A. Ghasemi, R. Shoja-Razavi and M. Tavousi, The role of pH on the particle size and magnetic consequence of cobalt ferrite, *J. Magn. Magn. Mater.*, 2015, **396**, 288–294.

42 G. A. El-Shobaky, A. M. Turky, N. Y. Mostafa and S. K. Mohamed, Effect of preparation conditions on physicochemical, surface and catalytic properties of cobalt ferrite prepared by coprecipitation, *J. Alloys Compd.*, 2010, **493**, 415–422.

43 J. Giri, T. Sriharsha and D. Bahadur, Optimization of parameters for the synthesis of nano-sized Co1−xZnxFe2O4, ($0 \leq x \leq 0.8$) by microwave refluxing, *J. Mater. Chem.*, 2004, **14**, 875–880.

44 M. Ristic, S. Krehula, M. Reissner, M. Jean, B. Hannoyer and S. Musić, Synthesis and properties of precipitated cobalt ferrite nanoparticles, *J. Mol. Struct.*, 2017, **1140**, 32–38.

45 S. Akbari, S. M. Masoudpanah, S. M. Mirkazemi and N. Aliyan, PVA assisted coprecipitation synthesis and characterization of MgFe2O4 nanoparticles, *Ceram. Int.*, 2017, **43**, 6263–6267.

46 A. L. Tiano, G. C. Papaefthymiou, C. S. Lewis, J. Han, C. Zhang, Q. Li, C. Shi, A. M. M. Abeykoon, S. J. L. Billinge, E. Stach, J. Thomas, K. Guerrero, P. Munayco, J. Munayco, R. B. Scorzelli, P. Burnham, A. J. Viescas and S. S. Wong, Correlating Size and Composition-Dependent Effects with Magnetic, Mössbauer, and Pair Distribution Function Measurements in a Family of Catalytically Active Ferrite Nanoparticles, *Chem. Mater.*, 2015, **27**, 3572–3592.

47 S. M. Ansari, B. B. Sinha, D. Phase, D. Sen, P. U. Sastry, Y. D. Kolekar and C. V. Ramana, Particle Size, Morphology, and Chemical Composition Controlled CoFe2O4 Nanoparticles with Tunable Magnetic Properties via Oleic Acid Based Solvothermal Synthesis for Application in Electronic Devices, *ACS Appl. Nano Mater.*, 2019, **2**, 1828–1843.

48 D. Zhao, X. Wu, H. Guan and E. Han, Study on supercritical hydrothermal synthesis of CoFe2O4 nanoparticles, *J. Supercrit. Fluids*, 2007, **42**, 226–233.

49 M. Ghanbari, F. Davar and A. E. Shalan, Effect of rosemary extract on the microstructure, phase evolution, and magnetic behavior of cobalt ferrite nanoparticles and its application on anti-cancer drug delivery, *Ceram. Int.*, 2021, **47**, 9409–9417.

50 Z. Mahhouti, H. El Moussaoui, T. Mahfoud, M. Hamedoun, M. El Marssi, A. Lahmar, A. El Kenz and A. Benyoussef, Chemical synthesis and magnetic properties of monodisperse cobalt ferrite nanoparticles, *J. Mater. Sci.: Mater. Electron.*, 2019, **30**, 14913–14922.

51 M. Rethinasabapathy, A. T. E. Vilian, S. K. Hwang, S.-M. Kang, Y. Cho, Y.-K. Han, J.-K. Rhee and Y. S. Huh, Cobalt ferrite microspheres as a biocompatible anode for higher power generation in microbial fuel cells, *J. Power Sources*, 2021, **483**, 229170.

52 M. M. El-Masry, R. Ramadan and M. K. Ahmed, The effect of adding cobalt ferrite nanoparticles on the mechanical properties of epoxy resin, *Results Mater.*, 2020, **8**, 100160.

53 H. S. Jahin, M. I. Kandil and M. Y. Nassar, Facile auto-combustion synthesis of calcium aluminate nanoparticles for efficient removal of Ni(II) and As(III) ions from wastewater, *Environ. Technol.*, 2022, 1–38.

54 M. Ramakrishna, D. Rajesh Babu, R. M. Gengan, S. Chandra and G. Nageswara Rao, Green synthesis of gold nanoparticles using marine algae and evaluation of their catalytic activity, *J. Nanostruct. Chem.*, 2016, **6**, 1–13.

55 P. B. Kharat, S. B. Somvanshi, P. P. Khirade and K. M. Jadhav, Induction Heating Analysis of Surface-Functionalized Nanoscale CoFe2O4 for Magnetic Fluid Hyperthermia toward Noninvasive Cancer Treatment, *ACS Omega*, 2020, **5**, 23378–23384.

56 Z. E. Gahrouei, S. Labbaf and A. Kermanpur, Cobalt doped magnetite nanoparticles: synthesis, characterization, optimization and suitability evaluations for magnetic hyperthermia applications, *Phys. E*, 2020, **116**, 113759.

57 S. Williams, C. L. Okolie, J. Deshmukh, L. Hawco, J. McNeil, A. C. Nganou Assonkeng, C. Bennett and M. Mkandawire, Magnetizing Cellulose Fibers with CoFe2O4 Nanoparticles for Smart Wound Dressing for Healing Monitoring Capability, *ACS Appl. Bio Mater.*, 2019, **2**, 5653–5662.

58 S. Ayyappan, S. Mahadevan, P. Chandramohan, M. P. Srinivasan, J. Philip and B. Raj, Influence of Co2+ Ion Concentration on the Size, Magnetic Properties, and Purity of CoFe2O4 Spinel Ferrite Nanoparticles, *J. Phys. Chem. C*, 2010, **114**, 6334–6341.

59 M. Kooti, A. N. Sedeh, K. Gheisari and A. Figuerola, Synthesis, characterization, and performance of nanocomposites containing reduced graphene oxide, polyaniline, and cobalt ferrite, *Phys. B*, 2021, **612**, 412974.

60 J. M. Arshad, W. Raza, N. Amin, K. Nadeem, M. I. Arshad and M. A. Khan, Synthesis and characterization of cobalt ferrites as MRI contrast agent, *Mater. Today: Proc.*, 2021, **47**, S50–S54.

61 F. H. Aragón, J. A. H. Coaquira, L. Villegas-Lelovsky, S. W. da Silva, D. F. Cesar, L. C. C. M. Nagamine, R. Cohen, E. Menéndez-Proupin and P. C. Morais, Evolution of the doping regimes in the Al-doped SnO_2nanoparticles prepared by a polymer precursor method, *J. Phys.: Condens. Matter*, 2015, **27**, 095301.

62 S. Gandhi, S. Issar, A. K. Mahapatro and I. Roy, Cobalt ferrite nanoparticles for bimodal hyperthermia and their mechanistic interactions with lysozyme, *J. Mol. Liq.*, 2020, **310**, 113194.

63 G. P. Ratkovski, K. T. O. do Nascimento, G. C. Pedro, D. R. Ratkovski, F. D. S. Gorza, R. J. da Silva, B. G. Maciel, L. C. Mojica-Sánchez and C. P. de Melo, Spinel Cobalt Ferrite Nanoparticles for Sensing Phosphate Ions in Aqueous Media and Biological Samples, *Langmuir*, 2020, **36**, 2920–2929.

64 B. Lakshmi, B. Joe Thomas and P. Gopinath, Accurate band gap determination of chemically synthesized cobalt ferrite nanoparticles using diffuse reflectance spectroscopy, *Adv. Powder Technol.*, 2021, **32**, 3706–3716.

65 M. Y. Nassar and S. Abdallah, Facile controllable hydrothermal route for a porous CoMn2O4 nanostructure: synthesis, characterization, and textile dye removal from aqueous media, *RSC Adv.*, 2016, **6**, 84050–84067.

66 M. Y. Nassar, A. A. Ali and A. S. Amin, A facile Pechini sol-gel synthesis of TiO2/Zn2TiO2/ZnO/C nanocomposite: an efficient catalyst for the photocatalytic degradation of Orange G textile dye, *RSC Adv.*, 2017, **7**, 30411–30421.

67 S. Swathi, R. Yuvakkumar, P. S. Kumar, G. Ravi and D. Velauthapillai, Annealing temperature effect on cobalt ferrite nanoparticles for photocatalytic degradation, *Chemosphere*, 2021, **281**, 130903.

68 J. P. Singh, J. Y. Park, V. Singh, S. H. Kim, W. C. Lim, H. Kumar, Y. H. Kim, S. Lee and K. H. Chae, Correlating the size and cation inversion factor in context of magnetic and optical behavior of CoFe2O4 nanoparticles, *RSC Adv.*, 2020, **10**, 21259–21269.

69 Y. Lu, M. Yousaf, M. N. Akhtar, A. Noor, M. Akbar, M. A. K. Y. Shah, S. Yan and F. Wang, Effect of Gd and Co contents on the microstructural, magneto-optical and electrical characteristics of cobalt ferrite (CoFe2O4) nanoparticles, *Ceram. Int.*, 2022, **48**, 2782–2792.

70 A. Miri, M. Sarani, A. Najafidoust, M. Mehrabani, F. A. Zadeh and R. S. Varma, Photocatalytic performance and cytotoxic activity of green-synthesized cobalt ferrite nanoparticles, *Mater. Res. Bull.*, 2022, **149**, 111706.

71 D. D. Andhare, S. R. Patade, J. S. Kounsalye and K. M. Jadhav, Effect of Zn doping on structural, magnetic and optical properties of cobalt ferrite nanoparticles synthesized via Co-precipitation method, *Phys. B*, 2020, **583**, 412051.

72 R. Behura, R. Sakthivel and N. Das, Synthesis of cobalt ferrite nanoparticles from waste iron ore tailings and spent lithium ion batteries for photo/sono-catalytic degradation of Congo red, *Powder Technol.*, 2021, **386**, 519–527.

73 A. V. Ravindra, M. Chandrika, C. Rajesh, P. Kollu, S. Ju and S. D. Ramarao, Simple synthesis, structural and optical properties of cobalt ferrite nanoparticles, *Eur. Phys. J. Plus*, 2019, **134**, 296.